ANCHORING DISTORTIONS COUPLED WITH PLANE COUETTE & POISEUILLE FLOWS OF NEMATIC POLYMERS IN VISCOUS SOLVENTS: MORPHOLOGY IN MOLECULAR ORIENTATION, STRESS & FLOW

Hong Zhou

Department of Applied Mathematics
Naval Postgraduate School
Monterey, California 93943-5216

M. Gregory Forest

Department of Mathematics & Institute for Advanced Materials
University of North Carolina at Chapel Hill
Chapel Hill, North Carolina 27599-3250

Abstract. The aim of this work is to model and simulate processing-induced heterogeneity in rigid, rod-like nematic polymers in viscous solvents. We employ a mesoscopic orientation tensor model due to Doi, Marrucci and Greco which extends the small molecule, liquid crystal theory of Leslie-Ericksen-Frank to nematic polymers. The morphology has various physical realizations, all coupled through the model equations: the orientational distribution of the ensemble of rods, anisotropic viscoelastic stresses, and flow feedback. Previous studies in plane Couette & Poiseuille flow (with the exception of [7]) have focused on the coupling between hydrodynamics and the orientational distribution of rigid rod polymers with identical anchoring conditions at solid boundaries; without flow, the equilibrium structure is homogeneous. Here we explore steady structures that emerge with mismatch anchoring conditions at the walls, which couple an equilibrium elastic distortion across the channel, short and long range elasticity potentials, and hydrodynamics. In plane Couette (where moving plates drive the flow) and Poiseuille flow (where a pressure gradient drives the flow), in the regime of weak flow and strong distortional elasticity, asymptotic analysis yields closed-form steady solutions and scaling laws with identical wall conditions. We focus simulations in this regime to expose the effects due to wall anchoring conflicts, and illustrate the induced morphology of the orientational distribution, stored viscoelastic stresses, and non-Newtonian flow. A remarkably simple diagnostic emerges in this physical parameter regime, in which salient morphology features are controlled by the amplitude and sign of the difference in plate anchoring angles of the director field at the two plates.

1. **Introduction.** In previous work [1, 9] the authors have studied steady structure scaling properties of nematic polymers in plane Couette cells (where imposed plate motion drives the system) and in plane Poiseuille flow (driven by an imposed pressure gradient). The model employed is a combination of the Doi-Hess theory for flowing rigid rod-like polymers in viscous solvents, together with the

Report Documentation Page

1. REPORT DATE **2006**	2. REPORT TYPE	3. DATES COVERED **00-00-2006 to 00-00-2006**

4. TITLE AND SUBTITLE **Anchoring Distortions Coupled with Plane Couette & Poiseuille Flows of Nematic Polymers in Viscous Solvents: Morphology in Molecular Orientation, Stress & Flow**	5a. CONTRACT NUMBER
	5b. GRANT NUMBER
	5c. PROGRAM ELEMENT NUMBER
6. AUTHOR(S)	5d. PROJECT NUMBER
	5e. TASK NUMBER
	5f. WORK UNIT NUMBER
7. PERFORMING ORGANIZATION NAME(S) AND ADDRESS(ES) **Naval Postgraduate School,Department of Applied Mathematics,Monterey,CA,93943-5216**	8. PERFORMING ORGANIZATION REPORT NUMBER
9. SPONSORING/MONITORING AGENCY NAME(S) AND ADDRESS(ES)	10. SPONSOR/MONITOR'S ACRONYM(S)
	11. SPONSOR/MONITOR'S REPORT NUMBER(S)

12. DISTRIBUTION/AVAILABILITY STATEMENT
Approved for public release; distribution unlimited

13. SUPPLEMENTARY NOTES

14. ABSTRACT

The aim of this work is to model and simulate processing-induced heterogeneity in rigid, rod-like nematic polymers in viscous solvents. We employ a mesoscopic orientation tensor model due to Doi, Marrucci and Greco which extends the small molecule, liquid crystal theory of Leslie-Ericksen-Frank to nematic polymers. The morphology has various physical realizations, all coupled through the model equations: the orientational distribution of the ensemble of rods, anisotropic viscoelastic stresses, and flow feedback. Previous studies in plane Couette & Poiseuille flow (with the exception of [7]) have focused on the coupling between hydrodynamics and the orientational distribution of rigid rod polymers with identical anchoring conditions at solid boundaries; without flow, the equilibrium structure is homogeneous. Here we explore steady structures that emerge with mismatch anchoring conditions at the walls, which couple an equilibrium elastic distortion across the channel, short and long range elasticity potentials, and hydrodynamics. In plane Couette (where moving plates drive the flow) and Poiseuille flow (where a pressure gradient drives the flow), in the regime of weak flow and strong distortional elasticity, asymptotic analysis yields closed-form steady solutions and scaling laws with identical wall conditions. We focus simulations in this regime to expose the effects due to wall anchoring conflicts, and illustrate the induced morphology of the orientational distribution, stored viscoelastic stresses, and non-Newtonian flow. A remarkably simple diagnostic emerges in this physical parameter regime, in which salient morphology features are controlled by the amplitude and sign of the difference in plate anchoring angles of the director field at the two plates.

15. SUBJECT TERMS

16. SECURITY CLASSIFICATION OF:			17. LIMITATION OF ABSTRACT	18. NUMBER OF PAGES	19a. NAME OF RESPONSIBLE PERSON
a. REPORT **unclassified**	b. ABSTRACT **unclassified**	c. THIS PAGE **unclassified**	**Same as Report (SAR)**	**19**	

Marrucci-Greco distortional elasticity potential. A second-moment tensor describes the orientational distribution of the ensemble of rod-like macromolecules, where the full kinetic theory for the distribution function is projected onto a second-moment description using closure rules. The experimental conditions and the model allow an assumption that the spatial variations in flow, orientation, and stress are one-dimensional, along the normal to the parallel walls. The mesoscopic model then admits a variety of analytical results, in particular an asymptotic analysis yields closed-form expressions for the flow and orientation tensor in the dual limit of slow flow and strong distortional elasticity. These results are based on identical anchoring conditions of the nematic liquid at both plates, which means the elastic distortion in the material arises upon inception of flow. This assumption is more for convenience than practical consideration; it allows one to use the large body of results on homogeneous nematic liquids (so-called monodomains) in imposed linear flows to guide the early structure evolution in experiments. In reality, nematic liquids are rarely free of heterogeneity, so this study is aimed toward an understanding of how flow generates structure evolution from a controlled quiescent equilibrium with distortions. An imposition of different anchoring conditions of the nematogens at parallel walls is a controllable condition for an experiment as well as in the model. In our numerical simulations, we will track the structure morphology versus degree of mismatch in the anchoring conditions for both experimental devices.

Effects of different wall anchoring conditions in liquid crystals, modeled by the Leslie-Ericksen-Frank equations, have been studied extensively, cf. the treatise of de Gennes & Prost [6]. The only nematic polymer studies we are aware of which simulate mismatches in wall anchoring conditions for nematic polymers are the recent lattice Boltzmann calculations for Couette flow by Marenduzzo, Orlandini, and Yeomans [17], based on a mesoscopic Beris-Edwards model similar to our Doi-Marrucci-Greco model. Their results are for full three dimensional simulations, presented in terms of morphology between the plates which offer direct comparisons to our posited one-dimensional results. They indicate a variety of phenomena which are consistent with our observations. The comparison suggests a certain robustness to higher dimensional effects of the layered features we restrict to. The parameter space of these experiments, and of tensorial and full kinetic theory models, is huge. As a result, the field remains far away from any coherent classification of types of morphology, and correlations, in the flow, orientational distribution, or stored stresses of nematic polymer films. Thus, we aim here to document phenomena which may be explored for experimental and model validation.

For this paper, we do not jump right to the full complexity of the high Ericksen number regime, which is the most physically relevant for liquid crystals and liquid crystal polymers. This approach has led to an impasse in the field. First, there are notorious numerical difficulties, and at high Ericksen numbers one has to set extremely low time and space tolerances just to get converged simulations. Secondly, there are simply too many "sources" of complex phenomena (orientational instabilities and shear banding and the question of their temporal and spatial correlations, persistence length of plate boundary layers and structure within those layers, spawning of defect cores) which need to be isolated and understood, and then coupled into an eventual simulation with full blown complexity. In this paper, we restrict our simulations to the regime of weak flow (realistic for processing applications) and strong elasticity (not realistic except perhaps during a thermal quench

phase). With this motivation and caveats, our goal is two-fold: to compare morphology features with exact analytical results for identical anchoring conditions; and to avoid the parameter regime of unsteady structures. The release of these conditions, as well as allowance for higher physical and orientational space dimensionality, are deferred to future studies.

The reader is also referred to important work on mesoscopic model simulations of structure in plane Couette flow, notably the work of Gary Leal and co-workers [20], Alejandro Rey and co-workers [21, 22], and Morton Denn and co-workers [15]. The reviews of Denn and Rey [19] and Kroger [16] provide valuable reading and background.

2. **Formulation.** Figure 1 illustrates the experimental setup for Couette (moving plates) and Poiseuille (pressure gradient with stationary plates) devices. For the channel flows shown in Fig. 1, the variations in physical space are limited to the direction y between the parallel plates, allowing for stratified nonlinear shear flow. For liquid crystals (LCs) and liquid crystal polymers (LCPs) confined between two aligning plates, there are two important properties of the orientational distribution of the rigid rod or platelet ensemble – elasticity and sensivitity to confining surfaces. LCs and LCPs have elasticity due to short-range excluded volume interactions and due to inhomogeneities, both of which cost energy when the nematic liquid is out of the favored homogeneous equilibrium distribution. At sufficient concentrations, the rest equilibrium is nematic, or ordered, with a peak direction called the major director that is free in the absence of a selection mechanism. Confining surfaces impose such a selection in the proximity of the surface, which is known as anchoring. In practice, anchoring conditions can be tuned by rubbing, controlling the surface temperature, and coating the plates with an amphiphilic material [6, 13].

Since liquid crystals are anisotropic viscoelastic materials, the modeling of these structured materials must take the orientational order into account. Both the short-range excluded volume potential and long-range distortional elasticity potential contribute "extra stresses", beyond the viscous stress and isotropic pressure. These stresses then drive the flow, which is the mechanism for flow feedback or non-Newtonian effects. In this paper we adopt the Doi-type tensor theory to study nematic polymers in viscous solvents. This model relies on the kinetic (diffusion) equation for a probability distribution function of a rodlike molecule in direction $\mathbf{m}$ at position $\mathbf{x}$ and time t. The probability distribution function $f(\mathbf{m}, \mathbf{x})$ of Doi-Hess kinetic theory is projected onto the second-moment tensor, $\mathbf{M}$, a symmetric, trace 1, positive semi-definite tensor of rank 2. The ordered eigenvalues d_i of $\mathbf{M}$ satisfy $0 \le d_3 \le d_2 \le d_1 \le 1, d_1 + d_2 + d_3 = 1$. The corrresponding ordered eigenvectors, $\mathbf{n}_i$ are the *directors* of the nematic liquid. The major director, $\mathbf{n}_1$, is the principal axis of orientation. Traditionally, $\mathbf{M}$ is normalized to trace 0 by subtracting a multiple of the identity tensor, defining the *orientation tensor* $\mathbf{Q} = \mathbf{M} - \frac{1}{3}\mathbf{I}$. The eigenvectors (directors) and corresponding differences in eigenvalues of $\mathbf{M}$ and $\mathbf{Q}$ are identical. The *order parameters*, $s = d_1 - d_2, \beta = d_2 - d_3$, describe the anisotropy of the orientational distribution of the rod-like molecular ensemble. Defects are phases of the liquid in which the major director is degenerate, or not uniquely defined, a necessary condition being $s = 0$, which includes the isotropic phase $\mathbf{Q} = \mathbf{0}$. It turns out that stable, homogeneous equilibrium phases are either isotropic (at low concentrations of rod-like molecules) or uniaxial, with $s > 0$, $\beta = 0$. These uniaxial phases are thereby prescribed at each solid plate, and can be controlled either chemically or mechanically (by rubbing).

The Doi-type kinetic theory couples the orientation effect to the flow through classical mechanics and kinetics principles. In this approach, the Newtonian stress law is extended to include flow-orientation coupling. The dimensionless forms of the balance of linear momentum, continuity equation, stress constitutive equation, and the time evolution equation for the orientation tensor due to Doi, Marrucci, and Greco are given as follows:

Balance of linear momentum:

$$\frac{d}{dt}\mathbf{v} = \nabla \cdot (-p\mathbf{I} + \tau), \tag{1}$$

where $\mathbf{v}$ is the velocity, p is the pressure, $\mathbf{I}$ is the unit tensor, and τ is the extra stress.

Continuity equation:

$$\nabla \cdot \mathbf{v} = 0. \tag{2}$$

Stress constitutive equation:

$$\begin{aligned}
\tau &= \left(\frac{2}{Re} + \mu_3\right)\mathbf{D} + a\,\alpha\,F(\mathbf{Q}) \\
&+ \frac{a\alpha}{3Er}\left\{\Delta\mathbf{Q}:\mathbf{Q}(\mathbf{Q}+\frac{\mathbf{I}}{3}) - \frac{1}{2}(\Delta\mathbf{Q}\mathbf{Q} + \mathbf{Q}\Delta\mathbf{Q}) - \frac{1}{3}\Delta\mathbf{Q}\right\} \\
&+ \frac{\alpha}{3Er}\left\{\frac{1}{2}(\mathbf{Q}\Delta\mathbf{Q} - \Delta\mathbf{Q}\mathbf{Q}) - \frac{1}{4}(\nabla\mathbf{Q}:\nabla\mathbf{Q} - \nabla\nabla\mathbf{Q}:\mathbf{Q})\right\} \\
&+ \mu_1\left\{(\mathbf{Q}+\frac{\mathbf{I}}{3})\mathbf{D} + \mathbf{D}(\mathbf{Q}+\frac{\mathbf{I}}{3})\right\} + \mu_2\mathbf{D}:\mathbf{Q}\left(\mathbf{Q}+\frac{\mathbf{I}}{3}\right),
\end{aligned} \tag{3}$$

where Re is the solvent Reynolds number, Er is the Ericksen number (large values correspond to weak distortional elasticity), μ_i $(i=1,2,3)$ are three nematic Reynolds numbers (normalized viscosities), $\mathbf{D}$ is the symmetric part of the velocity gradient tensor, also known as the rate of strain tensor, α is a normalized entropic parameter, a is a dimensionless parameter depending on the molecular aspect ratio r of spheroidal molecules

$$a = \frac{r^2 - 1}{r^2 + 1},$$

and the short-range excluded volume effects are captured by

$$F(\mathbf{Q}) = (1 - N/3)\mathbf{Q} - N\mathbf{Q}^2 + N\mathbf{Q}:\mathbf{Q}(\mathbf{Q}+\mathbf{I}/3), \tag{4}$$

where N is a dimensionless concentration of nematic polymers, which controls the strength of the mesoscopic approximation, $F(\mathbf{Q})$, of the gradient of the Maier-Saupe potential. For this paper, we use the following parameter values. First we set a nematic concentration $N = 6$, for which stable quiescent equilibria satisfying $F(\mathbf{Q}) = 0$ are uniaxial ($\beta = 0$), ordered phases with Flory order parameter s given below, equation (7). We select $a = 0.8$, or aspect ratio $r = 3$, which for the Doi closure gives excellent agreement with the full kinetic theory in the longwave limit of sheared monodomains [10, 11, 12]. Finally we set $\alpha = 2.0$, $\mu_1 = 2.3867 \times 10^{-4}$, $\mu_2 = 3.1667 \times 10^{-3}$, $\mu_3 = 3.5 \times 10^{-3}$, consistent with our previous papers [1, 9] so that we identify anchoring distortion effects; similarly, we use a constant rotational diffusivity. Here we choose parameters in the regime of weak flow and strong distortional elasticity where asymptotic analysis [9] yields closed-form steady solutions and scaling laws with identical wall conditions. We restrict our simulations to this regime to expose the effects of conflicting anchoring conditions, where we

have a baseline for comparison. Detailed studies of other parameter regimes will be explored in future work.

Orientation tensor equation:

$$
\begin{aligned}
\frac{d}{dt}\mathbf{Q} = \ & \mathbf{\Omega Q} - \mathbf{Q\Omega} + a\left[\mathbf{DQ} + \mathbf{QD}\right] + \frac{2a}{3}\mathbf{D} - 2a\mathbf{D} : \mathbf{Q}(\mathbf{Q} + \frac{\mathbf{I}}{3}) \\
& - \left\{ F(\mathbf{Q}) + \frac{1}{3Er}[\Delta\mathbf{Q} : \mathbf{Q}(\mathbf{Q} + \frac{\mathbf{I}}{3}) - \frac{1}{2}(\Delta\mathbf{Q}\mathbf{Q} + \mathbf{Q}\Delta\mathbf{Q}) - \frac{1}{3}\Delta\mathbf{Q}]\right\}.
\end{aligned}
\tag{5}
$$

Here $\mathbf{\Omega}$ is the vorticity tensor defined by

$$
\mathbf{\Omega} = \frac{1}{2}(\nabla\mathbf{v} - \nabla\mathbf{v}^T),
\tag{6}
$$

where $\mathbf{v}$ is the velocity field for the flowing LCP and the superscript T denotes the transpose of a second order tensor.

The boundary conditions for the velocity are scaled to

$$
\mathbf{v}|_{y=\pm 1} = \begin{cases} (\pm De, 0, 0), & \text{for Couette flow,} \\ (0, 0, 0), & \text{for Poiseuille flow,} \end{cases}
\tag{7}
$$

where De is the Deborah number, the ratio of the relaxation time relative to the time scale set by the moving plates in the weak shear experiment. In this study we assume homogeneous mesophase anchoring at the channel boundaries, given by

$$
\mathbf{Q}|_{y=\pm 1} = s_0(\mathbf{n}_\pm\mathbf{n}_\pm - \frac{\mathbf{I}}{3}), \ \ s_0 = \frac{1}{4}(1 + 3\sqrt{1 - \frac{8}{3N}}),
\tag{8}
$$

where s_0 is the stable uniaxial order parameter specified by the nematic concentration N, and $\mathbf{n}_\pm$ is the equilibrium uniaxial director at $y = \pm 1$, respectively. All simulations reported in this paper employ $N = 6$. Here we assume $\mathbf{n}_\pm$ are anchored at the channel boundaries at some experimentally dictated anchoring angle $\psi_0^\pm$ with respect to the flow direction,

$$
\mathbf{n}_\pm = (\cos\psi_0^\pm, \sin\psi_0^\pm, 0).
\tag{9}
$$

The standard terminology employed here is: $\psi_0^\pm = 0, \pi/2$ are called tangential and homeotropic anchoring, respectively, since the director lies parallel or normal to the plates; tilted anchoring describes any condition in between, $0 < \psi_0^\pm < \pi/2$.

Following our previous studies [1, 9] where we have analytical results to compare with, we consider in-plane mesophase orientation of the nematic liquid, with two directors of $\mathbf{Q}$ confined to the plane (x, y), but still admitting biaxiality. This constraint implies that the orientation tensor can be written in terms of directors and order parameters:

$$
\mathbf{Q} = s(y, t)(\mathbf{nn} - \frac{\mathbf{I}}{3}) + \beta(y, t)(\mathbf{n}^\perp\mathbf{n}^\perp - \frac{\mathbf{I}}{3}),
\tag{10}
$$

with the directors $\mathbf{n}, \mathbf{n}^\perp$ confined to the (x, y) plane and parametrized by the in-plane Leslie angle $\psi(y, t)$,

$$
\mathbf{n} = (\cos\psi, \sin\psi, 0), \mathbf{n}^\perp = (-\sin\psi, \cos\psi, 0).
\tag{11}
$$

The third director is rigidly constrained along the vorticity axis. With this biaxial representation (10) of $\mathbf{Q}$, the orientation tensor equation (5) can be written

explicitly in terms of the two order parameters (s, β) and the Leslie angle ψ:

$$
\begin{aligned}
\frac{\partial s}{\partial t} = & -\left\{ U(s) + \frac{2N}{3} s\beta(1+\beta-s) + \frac{2}{9Er}(s-\beta)\,g(s,\beta)\,(\frac{\partial\psi}{\partial y})^2 \right. \\
& \left. + \frac{1}{9Er}\left[-(1-s)(1-\beta+2s)\frac{\partial^2 s}{\partial y^2} + s(1-s+2\beta)\frac{\partial^2\beta}{\partial y^2} \right] \right\} \\
& + \frac{a}{3}\frac{\partial v_x}{\partial y}\,g(s,\beta)\,\sin 2\psi, \\
\frac{\partial\beta}{\partial t} = & -\left\{ U(\beta) + \frac{2N}{3} s\beta(1+s-\beta) + \frac{2}{9Er}(\beta-s)\,g(\beta,s)\,(\frac{\partial\psi}{\partial y})^2 \right. \\
& \left. + \frac{1}{9Er}\left[\beta(1-\beta+2s)\frac{\partial^2 s}{\partial y^2} - (1-\beta)(1-s+2\beta)\frac{\partial^2\beta}{\partial y^2} \right] \right\} \\
& - \frac{a}{3}\frac{\partial v_x}{\partial y}\,g(\beta,s)\,\sin 2\psi, \\
\frac{\partial\psi}{\partial t} = & \;\frac{1}{6(s-\beta)}\left\{ \frac{\partial v_x}{\partial y}(3\beta-3s+a(2+s+\beta)\cos 2\psi) \right. \\
& \left. + \frac{1}{3Er}(2+s+\beta)\left[(s-\beta)\frac{\partial^2\psi}{\partial y^2} + 2\frac{\partial\psi}{\partial y}(\frac{\partial s}{\partial y} - \frac{\partial\beta}{\partial y}) \right] \right\},
\end{aligned}
\tag{12}
$$

where

$$
\begin{aligned}
U(s) &= s[1 - \frac{N}{3}(1-s)(2s+1)], \tag{13} \\
g(s,\beta) &= 1 + 3s\beta - \beta + 2s - 3s^2. \tag{14}
\end{aligned}
$$

The momentum equation simplifies to a single equation for the velocity component v_x along the primary flow direction,

$$
\begin{aligned}
\frac{\partial v_x}{\partial t} &= \frac{\partial\tau_{xy}}{\partial y}, \quad \text{for Couette flow} \\
\frac{\partial v_x}{\partial t} &= \frac{\partial\tau_{xy}}{\partial y} - \epsilon, \quad \text{for Poiseuille flow} \\
\tau_{xy} = & \;\frac{a\,\alpha}{2}\left[U(s) - U(\beta) + \frac{4\,Ns\beta}{3}(\beta-s) \right]\sin 2\psi \\
& + \frac{a\alpha}{18Er}\left[-h(s,\beta)\frac{\partial^2 s}{\partial y^2} + h(\beta,s)\frac{\partial^2\beta}{\partial y^2} \right. \\
& \left. + 2(s-\beta)(g(s,\beta)+g(\beta,s))(\frac{\partial\psi}{\partial y})^2 \right]\sin 2\psi \\
& + \frac{a\alpha}{18Er}(s+\beta+2)[(\beta-s)\frac{\partial^2\psi}{\partial y^2} - 2(\frac{\partial s}{\partial y} - \frac{\partial\beta}{\partial y})\frac{\partial\psi}{\partial y}]\cos 2\psi \\
& + \frac{\alpha}{6Er}(s-\beta)[(s-\beta)\frac{\partial^2\psi}{\partial y^2} + 2(\frac{\partial s}{\partial y} - \frac{\partial\beta}{\partial y})\frac{\partial\psi}{\partial y}] \\
& + \left[\frac{\mu_1}{6}(s+\beta+2) + \frac{\mu_2}{8}(s-\beta)^2(1-\cos 4\psi) + \frac{1}{Re} + \frac{\mu_3}{2} \right]\frac{\partial v_x}{\partial y},
\end{aligned}
\tag{15}
$$

where

$$
h(s,\beta) = (1-\beta+2s)(1+\beta-s). \tag{16}
$$

We seek steady solutions of the dimensionless Eqs. (12)-(16) subject to the boundary conditions

$$
s|_{y=\pm 1} = s_0, \quad \beta|_{y=\pm 1} = 0, \quad \psi|_{y=+1} = \psi_0^+, \quad \psi|_{y=-1} = \psi_0^-, \tag{17}
$$

and

$$
v_x|_{y=\pm 1} = \begin{cases} \pm De, & \text{for Couette flow} \\ 0, & \text{for Poiseuille flow.} \end{cases} \tag{18}
$$

3. **Numerical Results.** Figure 1 gives schematic diagrams for Couette and Poiseuille flow. The schematic flow profiles are Newtonian, which are typically posited in studies which suppress flow feedback. As noted earlier, one of our principal aims is to clarify the flow feedback induced by the extra stress, and the spatial correlations between the orientational distribution, stresses, and flow. Recall the second moment tensor $\mathbf{M}$ uniquely defines a triaxial ellipsoid with principal axes $\mathbf{n}_i$ with semi-axes lengths d_i. The projection of this ellipsoid onto the shear plane (x-y) is depicted in these schematics, showing a distortion in the principal axes across the gap; we are further interested in the focusing and defocusing of the orientational distribution, which will be captured by distortions in the order parameters and thereby in the shape of the ellipsoid. The schematic pictures show identical anchoring at the plates; the simulations will explore contrasts in anchoring conditions.
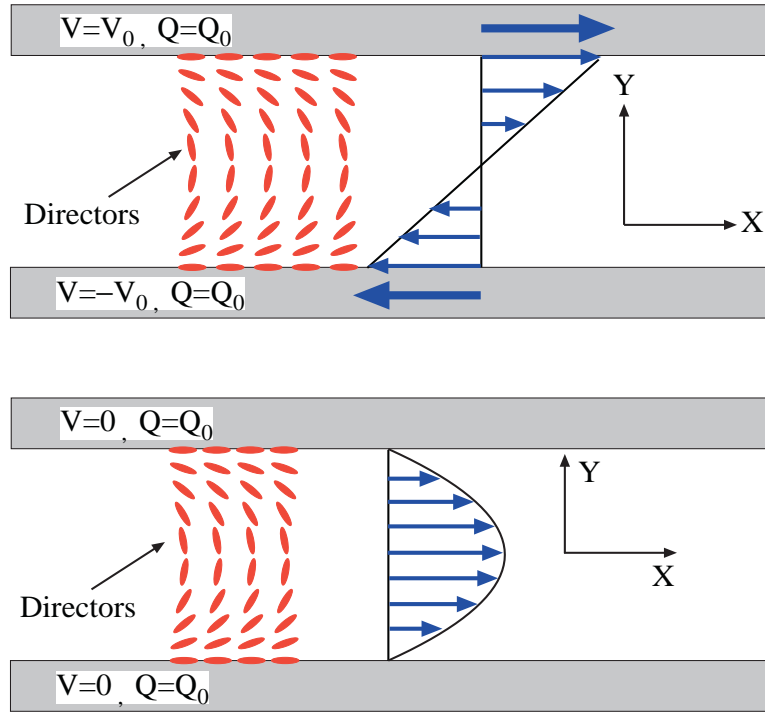

FIGURE 1. A schematic of the Couette flow (top) and Poiseuille flow (bottom) setup with fixed tangential anchoring conditions at both plates ($\psi_0^{+/-} = 0$).

The simulations reported here aim to highlight the coupling of weak flow and anchoring distortions, for plate or drag-driven flow (Figures 2-4) and pressure-driven flow (Figures 5-7). All figures are organized to visually distinguish each effect in isolation and then their interaction. The anchoring distortion is parametrized by the difference in imposed director angles at the plates:

$$\Delta \psi_0 = \psi_0^+ - \psi_0^-. \tag{19}$$

The device driving mechanisms are parametrized by the Deborah number, De, in Couette flow for Figures 2-4, and by the normalized pressure gradient ϵ in Poiseuille

flow, Figures 5-7. Column 1 in all figures suppresses anchoring distortions, either imposing weak flows $De = 0.1$ in Figures 2-4 or weak pressure gradients $\epsilon = 0.1$ in Figures 5-7. Column 3 suppresses hydrodynamics ($De = 0$ or $\epsilon = 0$) to illustrate pure anchoring distortions for two anchoring mismatch conditions, chosen from $\Delta\psi_0 = \pi/6, \pi/3, \pi/2$. Then the middle Column 2 exhibits coupled flow-anchoring distortion interactions. The discussions for each type of flow consist of comparisons of Columns 1 and 2 to glean the effects of anchoring mismatch conditions on weak flow structures developed previously [1, 9] for identical plate anchoring conditions, then comparisons of Columns 2 and 3 to ascertain the perturbative effect of weak flow on pure anchoring distortions.

The rows of each figure provide the various descriptive variables of the anisotropic nematic polymer liquid. Rows 1-5 give, in order, the gap structure between the bottom plate ($y = -1$) and top plate ($y = +1$) in: the major director angle ψ in the x-y plane; the departure $s - s_0$ of the uniaxial order parameter from equilibrium value at the plates; the biaxiality order parameter β; the primary flow component v_x; the first normal stress difference $N_1 = \tau_{11} - \tau_{22}$; and the shear stress τ_{12}.

3.1. Morphology for Couette flow.

Figures 2-4 illustrate flow-nematic steady state solutions and stored elastic stresses for plane Couette flow. We impose $Er = 1$ in all simulations to make contact with our previous analytical and numerical results [9] for identical plate conditions in weak flow ($De = 0.1$), depicted in Column 1 of each Figure. The purpose of three Figures 2-4 is to illustrate variability due solely to changes in the lower plate anchoring angle, with all other conditions the same.

We begin with Figure 2, which imposes tangential anchoring ($\psi_0^- = 0$) on the lower plate in all simulations. Column 1 imposes the same condition at the upper plate; Columns 2 and 3 show two different upper plate mismatch conditions, $\psi_0^+ = \pi/6$ (dashed) and $\pi/2$ (dotted). An immediate conclusion from comparison of Columns 1-3 is that anchoring distortions dominate weak flow effects. This is not surprising, since we have imposed order one distortions in the director field across the gap, with $\Delta\psi_0 = \pi/6$ and $\pi/2$, respectively, whereas the plate motion is asymptotically small ($De = 0.1$). The small parabolic distortion of the major director in Column 1 is two orders of magnitude weaker than the imposed anchoring mismatch distortion. This result has relevance in highly heterogeneous nematic polymer films, for example, which are riddled with defects that essentially impose strong anchoring distortions in the interstitial regions between them. One concludes that only strong flows are capable of modifying defect-ridden morphology.

Column 3 provides interesting insight into pure anchoring distortions. Some time ago, the authors [7, 8] investigated exact solutions of these mesoscopic model equations without flow, $De = 0$. The goal was to see which equilibrium structures could arise in the competition between short-range excluded volume and long-range distortional potentials. We were able to construct families of exact solutions by positing a separable form of the orientation tensor, in which we either froze the order parameters or froze the director field. These were *free space* solutions, absent of boundary conditions as asserted in Column 3. We speculated at that time that boundary conditions were necessary as selection mechanisms among these parametric families of solutions, and even anticipated that the exact separability would be modified. Remarkably, the pure anchoring distortions of Column 3 provide an example where boundary-anchoring conditions select a number of the special free-space solutions dominated by distortional (director) elasticity. Note the order parameter

variations across the gap from the equilibrium values at the plates, $(s, \beta) = (s_0, 0)$, are extremely weak.

Perhaps the most intriguing result of Figure 2 is the non-Newtonian flow feedback captured by Row 4. For equal plate anchoring conditions, it was shown in [9] that the leading order flow for oppositely moving parallel plates is Newtonian, i.e., simple linear shear; that is revealed in Column 1 of Row 4. Column 3 is of course the quiescent zero flow for stationary plates. Column 2 shows the remarkable nonlinear shear induced by the plate anchoring distortions of the director field. The stronger the distortion across the plate gap, i.e. as $\Delta\psi_0$ increases in absolute value, the stronger the flow field is modified. We emphasize that the flow feedback effect portrayed by these graphs is quite dramatic, and suggestive of a macroscopic flow control by switching of the boundary anchoring conditions.

Another non-Newtonian flow feature we point to is the expected behavior at the midgap, which is the Newtonian transition point from fluid moving to the right with the upper plate to fluid moving to the left with the lower plate. This zero flow transition point in the plate gap has shifted significantly toward the lower plate. This symmetry breaking in the flow field is induced by anchoring mismatch conditions! The macroscopic flow effect is remarkable: the top plate with these anchoring conditions entrains a very large layer which moves like plug flow at nearly the top plate speed. Then, because the mean shear rate across the gap has to equal the plate-imposed Deborah number, a rapid transition layer forms near the lower plate. The size of the top, fast-moving plug layer scales with the anchoring distortion between the plates, while the bottom rapid transition layer scales inversely with the degree of plate distortion.

Rows 5, 6 address the rheological perspective of stored stresses in these materials. In Figure 2, the shear stress, Row 6, is constant across the gap, and only non-zero with flow. This feature is upheld for each Couette simulation, primarily because of the low De corresponding to slow plate motion, which translates to relatively small gradients in local shear rate across the gap. (The Poiseuille simulations will enhance shear stress variations because of stronger local gradients in shear rate.) The first normal stress difference, N_1, Row 5, is negligible for identical anchoring conditions, then jumps 4 orders of magnitude with anchoring distortions. The morphology in N_1 correlates with the order parameter distortions, with amplitudes proportional to the difference $\Delta\psi_0$; this effect cannot be resolved without the short-range excluded volume potential of the Doi-Hess theory.

Figures 3 and 4 explore possible sensitivity, by comparison with Figure 2, due solely to changes in the anchoring angle at the lower plate relative to the flow and flow gradient directions. This investigation is motivated by results in [9] for matching plate conditions in weak flow ($De = 0.1$), duplicated in Column 1, Figures 2-4. Observe that tilted (Figure 3) and normal (Figure 4) anchoring at the lower plate amplify the boundary layer distortions in order parameters of Figure 2 by an order of magnitude; N_1 inherits the boundary layers at each plate.

We now move to the new results in Figures 3 and 4, involving plate anchoring distortions, discussing Figure 3 first. Column 3, Rows 1-3 show pure anchoring mismatch distortions without flow yield comparable amplitude variations in s, β, ψ as Column 1 due to weak flow without anchoring distortions. However, the relative signs of these orientation tensor features are the same if $\Delta\psi_0 > 0$, whereas they are opposite if $\Delta\psi_0 < 0$! Thus, when weak flow and anchoring distortions are coupled in Column 2, the opposing variations lead to non-convex distortions in

the order parameters s, β for $\Delta\psi_0 < 0$. The director distortions from the plate conditions are much stronger than the weak flow-induced distortions, which yield perturbative corrections to Column 3. Since the first normal stress difference, N_1, tracks the morphology of the order parameters, it also has non-convex variations for $\psi_0^+ = 0$, where $\Delta\psi_0 < 0$. Once again, the most dramatic effects are seen in Row 4, Column 2, where the flow concavity is non-linear as with Figure 2. A new feature is exposed in Figure 3, however: the flow profile switches concavity with a switch in sign of the anchoring mismatch condition, $\Delta\psi_0 < 0$ for tangential upper plate anchoring (dashed) versus $\Delta\psi_0 > 0$ for homeotropic upper plate anchoring (dotted). *This represents a macroscopic flow response to $sgn(\Delta\psi_0)$ in the weak flow limit, where zero mismatch yields a Newtonian shear profile, whereas mismatch plate conditions yield non-Newtonian flow profiles of opposite concavity.* The flow profiles have nearly plug flow near one plate and strong gradients in the local shear rate near the other plate. Once one convex profile is established, the other can also be induced by symmetry considerations. Absent of effects of gravity, there is no physical distinction in this problem between the top and bottom plates. Note further the significant elastic stress profile variations in N_1 and τ_{12} (Rows 4 & 5, Column 2 of Figure 3). The sign of $\Delta\psi_0$ leads to a doubling in amplitude of N_1 as well as non-convexity across the plate gap, similar to the structure of the order parameters. The shear stress is likewise strongly amplified by one sign of the anchoring mismatch, and negligible otherwise!

Figure 4 maintains a normal lower plate anchoring, and repeats the simulations of Figures 2 and 3. There are no essential differences in the orientation tensor features, except one notes the result from [9] in which the order parameters for equal anchoring conditions have extra structure. This was shown analytically to arise from a cancellation between the boundary layer structures and the structure that spans the plates; see [9]. The main feature we glean from Figure 4 is in the velocity profile, Row 4, Column 2. We observe the same concavity in v_x for both plate mismatch conditions, since each have $\Delta\psi_0 < 0$.

Putting the 3 figures together, we see that $sgn(\Delta\psi_0)$, the signum of the relative difference in director anchoring between the plates, controls convexity of the non-Newtonian flow feedback in this parameter regime of weak Couette flow.

3.2. **Morphology for Poiseuille flow.** Figures 5-7 illustrate gap structures for Poiseuille flow, with the same parameter studies as Figures 2-4 except the normalized plate speed De is replaced by the normalized pressure gradient ϵ. Columns 1 and 2 correspond to weak pressure gradient, $\epsilon = 0.1$, while Column 3 is the pure anchoring-induced distortion without flow, $\epsilon = 0$, identical to Column 3 of Figures 2-4.

We comment upon those features which are specific to Poiseuille flow. First, weak pressure gradient effects with equal plate anchoring conditions (Column 1) produce three orders of magnitude weaker variations than pure anchoring distortions with zero pressure gradient (Column 3) in all orientation features, s, β, ψ. The primary effect of their coupling, Column 2, Rows 1-3, is a weak symmetry-broken orientational morphology across the gap; it is not as dramatic as the Couette flow predictions due to the relative weakness of the pressure-driven responses.

The Newtonian Poiseuille flow profile of Column 1, obviously absent in Column 3 where $\epsilon = 0$, provides the preconditions for more significant flow feedback effects, and thereby stress phenomena. Column 2 illustrates two remarkable non-Newtonian flow features due to the coupling of pressure-gradients with anchoring distortions.

First, there is a symmetry-breaking in the flow profile which shifts the peak velocity (or zero gradient) toward one of the plates, by a significant distance proportional to $|\Delta\psi_0|$, toward the top plate if $\Delta\psi_0 < 0$ and toward the bottom plate if $\Delta\psi_0 > 0$. These effects are illustrated in Figures 5-7, Row 4. Second, anchoring distortions can either weaken (if $\Delta\psi_0 > 0$) or strengthen (if $\Delta\psi_0 < 0$) the flow, by significant percentages that are proportional to $|\Delta\psi_0|$! In Figure 5, note approximately 20% and 50% drops in flow strength across the gap induced by anchoring distortions with $\Delta\psi_0 > 0$, a similar result in the dotted graph of Figure 6, Row 4, Column 2, to be contrasted with comparable increases in flow strength across the gap induced by $\Delta\psi_0 < 0$ in the dashed curve of Figure 6, Row 4, Column 2 and both curves in Figure 7, Row 4, Column 2.

The first normal stress difference, N_1, Row 5 of Figures 5-7, shows similar significant features due to the coupling of pressure-driven flow and anchoring distortions, displayed in Column 2. Absent of this coupling, $N_1 > 0$ for pure anchoring distortions, Column 3, with values on the order of $0.1 - 0.2$. The weak pressure-driven values of N_1 are 3-4 orders of magnitude lower for weak Poiseuille flow and matching tangential or normal anchoring at each plate (Figures 5, 7, Column 1, Row 5). Tilted anchoring at both plates in weak flow, Figure 6, Row 5, Column 1, yields strongly enhanced N_1, with odd symmetry between the plates and mean zero. Then with coupling of pressure gradients and anchoring distortions, all Poiseuille simulations yield asymmetric first normal stress differences, with shifts in the gap location and amplitude of maximum N_1. The trends are more involved than a simple diagnostic such as $\text{sgn}(\Delta\psi_0)$, as with the velocity profile. In cases where N_1 across the gap is relatively small due to weak anchoring distortions and flow, Figure 5, Column 1 and 3, Row 5, the coupling can lead to sign changes in N_1 across the gap.

The shear stress, which is proportional to the gradient of v_x, is consistent with the gradient of Row 4 in all figures, and presents no surprises.

Concluding Remarks. Heterogeneity in the orientational distribution of nematic polymer ensembles in viscous solvents has been modeled for plane Couette and Poiseuille flows. This study has a particular focus on the coupling of anchoring-induced distortions at solid walls with weak drag-driven or pressure-driven flow. We have identified remarkable non-Newtonian flow and stress features generated in these conditions. The most dramatic effect is the degree to which the symmetry breaking of the plate anchoring conditions across the gap induces asymmetric macroscopic flow profiles and first normal stress differences. Furthermore, the degree of asymmetry and location of peak velocity relative to the plates can be switched by modifying the amplitude and sign in the difference between the plate anchoring angles of the major director of the orientation distribution. These results, if validated experimentally, suggest intriguing potential applications. For example, if the anchoring conditions were controllable by applied fields at solid walls, such as electric or magnetic fields, then one might consider switching boundary anchoring conditions to effect macroscopic flow and internal stress modifications.

The implications of these flow feedback phenomena at realistic distortional elasticity constants, i.e., much higher Ericksen numbers, are likely to be confined in short lengthscale boundary layers of size Er^p, where $0 < p < 1$, according to asymptotic scaling laws [1, 9]. It remains to be explored how these boundary layers penetrate into the interior during confined processing flows and influence bulk flow and stored stress profiles. Another issue remains to be addressed in the future is the

non-uniqueness and multistability under hybrid anchoring conditions, even though this problem has been considered for identical anchoring conditions [2, 3, 4, 14, 18]. We anticipate multiple states with these hybrid boundary conditions, but thus far we have not pursued this issue. In particular, it is highly likely that there will be confined in-plane structures together with out-of-plane structures, just like we have found in our simulations with symmetric anchoring conditions. How those multiple states evolve due to mismatches in anchoring is a topic we have only started to explore. The studies presented here afford a glimpse into the delicate morphology coupling that is possible in confined flows of nematic (rigid rod or platelet) dispersions. The authors and collaborators have only begun to use homogenization theory of high-aspect-ratio spheroidal inclusions to transfer these flow-induced morphologies in the orientation distribution and stored anisotropic stresses to infer bulk nano-composite material properties [23, 24, 25]. The anisotropic property tensors associated with structures shown here provide a theoretical basis for understanding performance features of high performance nematic polymer materials. In this regard, while these structures are determined in idealized model simulations, they are a natural starting point to explore the huge parameter space of nano-composite processing conditions.

<div align="center">

REFERENCES

</div>

[1] Z. Cui, M.G. Forest, Q. Wang, and H. Zhou, *On weak plane Couette and Poiseuille flows of rigid rod and platelet ensembles*, to appear in SIAM J. Appl. Math. (2006).

[2] P.K. Currie, *Couette flow of a nematic liquid crystal in the presence of a magnetic field*, Arch. Ration. Mech. Anal., **37** (1970), 222–242.

[3] P.K. Currie, and G.P. Macsithigh, *The stability and dissipation of solutions for shearing flow of nematic liquid crystals*, Q. J. I. Mech. Appl. Math., **32** (1979), 499–511.

[4] L.R.P. de Andrade Lima and A.D. Rey, *Poiseuille flow of Leslie-Ericksen discotic liquid crystals: solution multiplicity, multistability, and non-Newtonian rheology*, J. Non-Newtonian Fluid Mech., **110** (2003), 103–142.

[5] M. Doi and S.F. Edwards, The Theory of Polymer Dynamics, Oxford University Press, London, 1986.

[6] P.G. de Gennes and J. Prost, The Physics of Liquid Crystals, Oxford University Press, Oxford, 1993.

[7] M.G. Forest, Q. Wang, and H. Zhou, *Exact banded patterns from a Doi-Marrucci-Greco model of nematic liquid crystal polymers*, Phys. Rev. E, *61* (2000), 6655–6662.

[8] M.G. Forest, Q. Wang, and H. Zhou, *Methods for the exact construction of mesoscale spatial structures in liquid crystal polymers*, Phys. D, **152-153** (2001), 288–309.

[9] M.G. Forest, Q. Wang, H. Zhou, and R. Zhou, *Structure scaling properties of confined nematic polymers in plane Couette cells: The weak flow limit*, J. Rheol., **48** (2004), 175–192.

[10] M.G. Forest and Q. Wang, *Monodomain response of finite-aspect ratio macromolecules in shear and related linear flows*, Rheol. Acta, **42** (2003), 20–46.

[11] M.G. Forest, R. Zhou and Q. Wang, *The weak shear phase diagram for nematic polymers*, Rheol. Acta, **43** (2004), 17–37.

[12] M.G. Forest, R. Zhou and Q. Wang, *The flow-phase diagram of Doi-Hess theory for sheared nematic polymers II: finite shear rates*, Rheol. Acta, **44** (2004), 80–93.

[13] Ch. Gahwiller, *Temperature dependence of flow alignment in nematic liquid crystals*, Phys. Rev. Lett., **28** (1972), 1554–1556.

[14] W.H. Han, and A.D. Rey, *Supercritical bifurcations in simple shear flow of a non-aligining nematic: reactive parameter and director anchoring effects*, J. Non-Newtonian Fluid Mech., **48** (1993), 181–210.

[15] R. Kupferman, M. Kawaguchi and M.M. Denn, *Emergence of structure in a model of liquid crystalline polymers with elastic coupling*, J. Non-Newt. Fluid Mech., **91** (2000), 255–271.

[16] M. Kroger, *Simple models for complex nonequilibrium fields*, Physics Reports, **390** (2004), 453–551.

[17] D. Marenduzzo, E. Orlandini, and J.M. Yeomans, *Interplay between shear flow and elastic deformations in liquid crystals*, J. Chem. Phys., **121** (2004), 582–591.

[18] J.G. McIntosh, F.M. Leslie, and D.M. Sloan, *Stability for shearing flow of nematic liquid crystals*, Continuum Mech. Thermodyn., **9** (1997), 293–308.

[19] A.D. Rey and M.M. Denn, *Dynamical phenomena in liquid-crystalline materials*, Annual Rev. Fluid Mech., **34** (2002), 233–266.

[20] G. Sgalari, L.G. Leal and J. Feng, *The shear flow behavior of LCPs based on a generalized Doi model with distortional elasticity*, J. Non-Newt. Fluid Mech., **102** (2002), 361–382.

[21] T. Tsuji and A. D. Rey, *Effect of long range order on sheared liquid crystalline polymers, Part 1: compatibility between tumbling behavior and fixed anchoring*, J. Non-Newt. Fluid Mech., **73** (1997), 127–152.

[22] T. Tsuji and A. D. Rey, *Orientation mode selection mechanisms for sheared nematic liquid crystalline materials*, Phys. Rev. E, **57** (1998), 5609–5625.

[23] X.Y. Zheng, M.G. Forest, R. Lipton, R. Zhou, and Q. Wang, *Exact scaling laws for electrical conductivity properties of nematic polymer nano-composite monodomains*, Advanced Functional Materials, **15** (2005), 627–638.

[24] H. Zhou, M.G. Forest, X. Zheng, Q. Wang, and R. Lipton, *Extension-enhanced conductivity of liquid crystalline polymer nano-composites*, to appear in Macromolecular Symposia (2006).

[25] M. G. Forest, R. Zhou, Q. Wang, X. Zheng, and R. Lipton, *Anisotropy and heterogeneity of nematic polymer nano-composite film properties*, to appear in IMA Proceedings of September, 2004 Workshop on Soft Matter, U. Minnesota (2005).

E-mail address: `hzhou@nps.navy.mil`
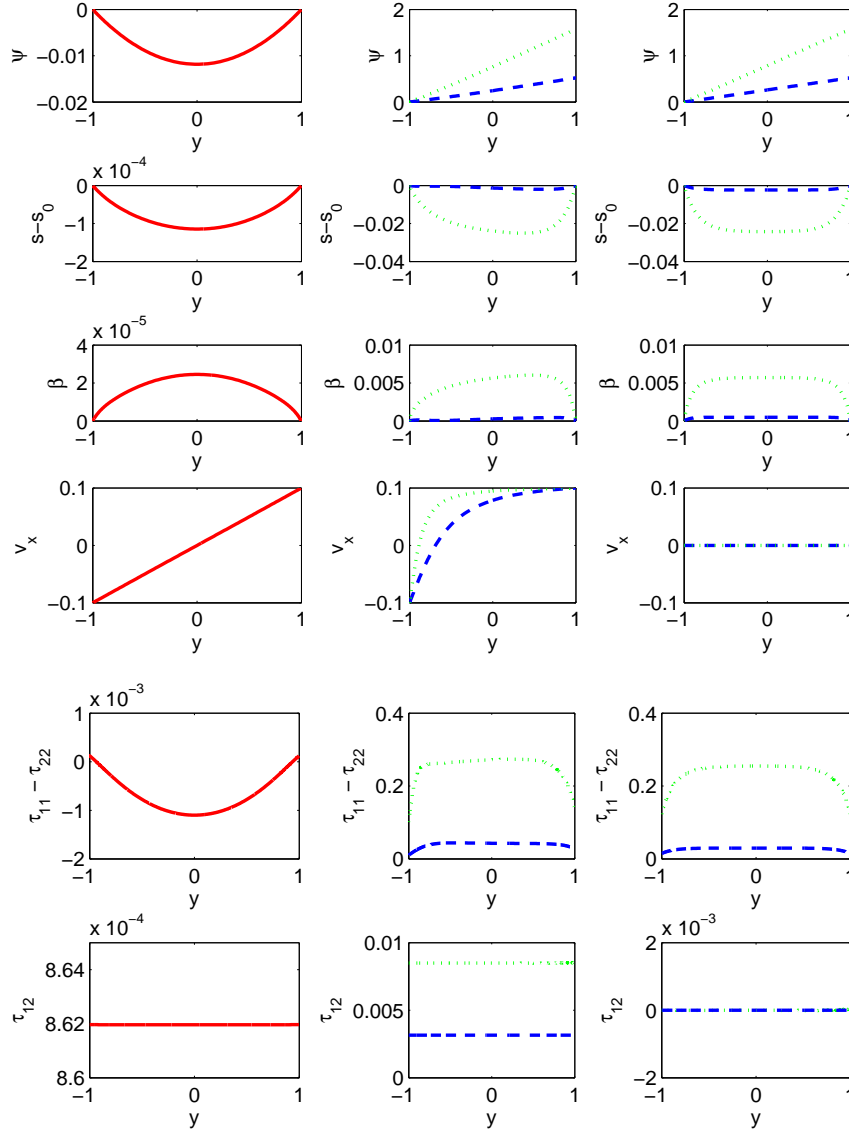*E-mail address*: `forest@amath.unc.edu`

FIGURE 2. Flow-nematic steady state solutions and associated stored elastic stresses for plane Couette flow, with $Er = 1$ held constant in all simulations, and fixed tangential anchoring at the lower plate ($\psi_0^- = 0$). Columns 1 and 2 impose weak plate motion, with $De = 0.1$; Column 3 gives the pure anchoring-induced distortional structures without flow ($De = 0$). Column 1 has identical plate conditions; Columns 2 and 3 show two different upper plate conditions, $\psi_0^+ = \frac{\pi}{6}$ (dashed) and $\frac{\pi}{2}$ (dotted). Rows 1-5 give, in order, the gap structure between the bottom plate ($y = -1$) and top plate ($y = +1$) in: the major director angle ψ in the x-y plane; the departure $s - s_0$ of the uniaxial order parameter from equilibrium value at the plates; the biaxiality order parameter β; the primary flow component v_x; the first normal stress difference $\tau_{11} - \tau_{22}$; and the shear stress τ_{12}.
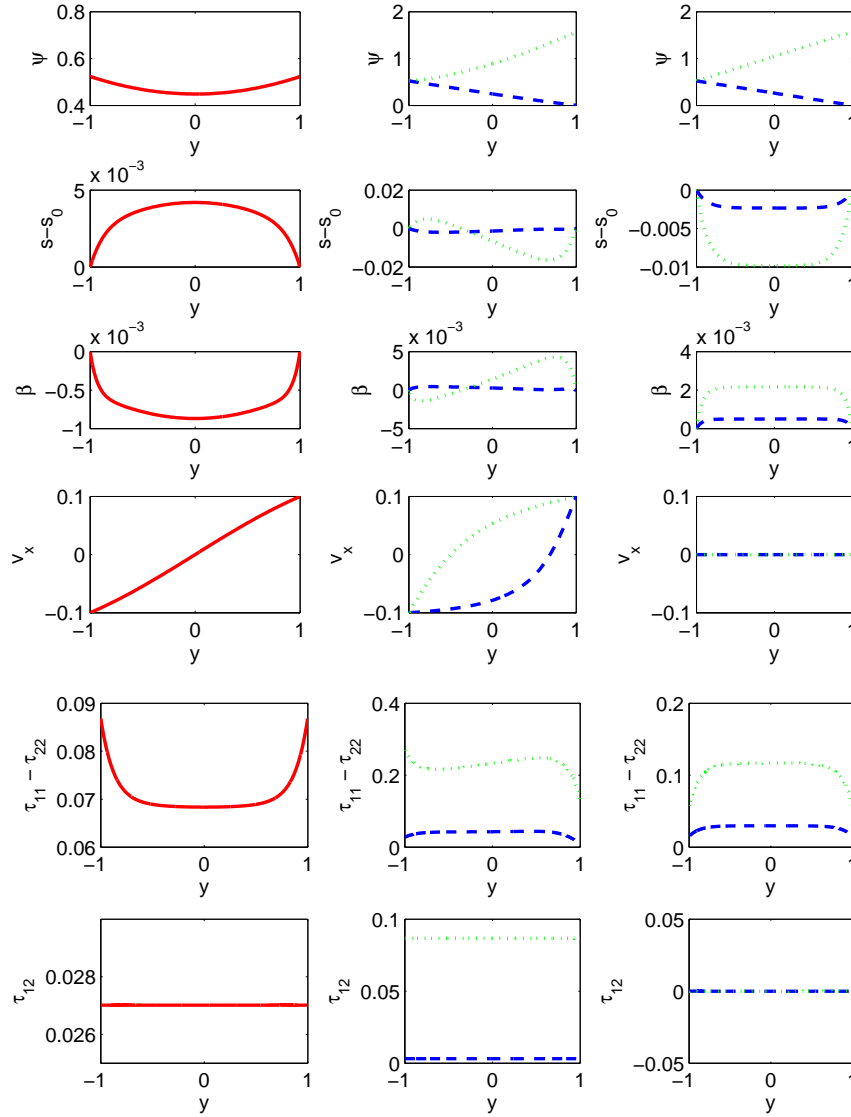
FIGURE 3. Couette flow structures, all with $Er = 1$, following Figure 2 except the lower plate is always maintained at the tilted anchoring condition $\psi_0^- = \frac{\pi}{6}$. Column 1 gives results for identical conditions at the top plate and slow flow $De = 0.1$. Column 3 gives results for zero flow $De = 0$, Column 2 with slow flow $De = 0.1$, for two different anchoring mismatches $\psi_0^+ = 0$ (dashed) and $\frac{\pi}{2}$ (dotted). Rows 1-5 depict the same orientational, flow, and stress variables as Figure 2.
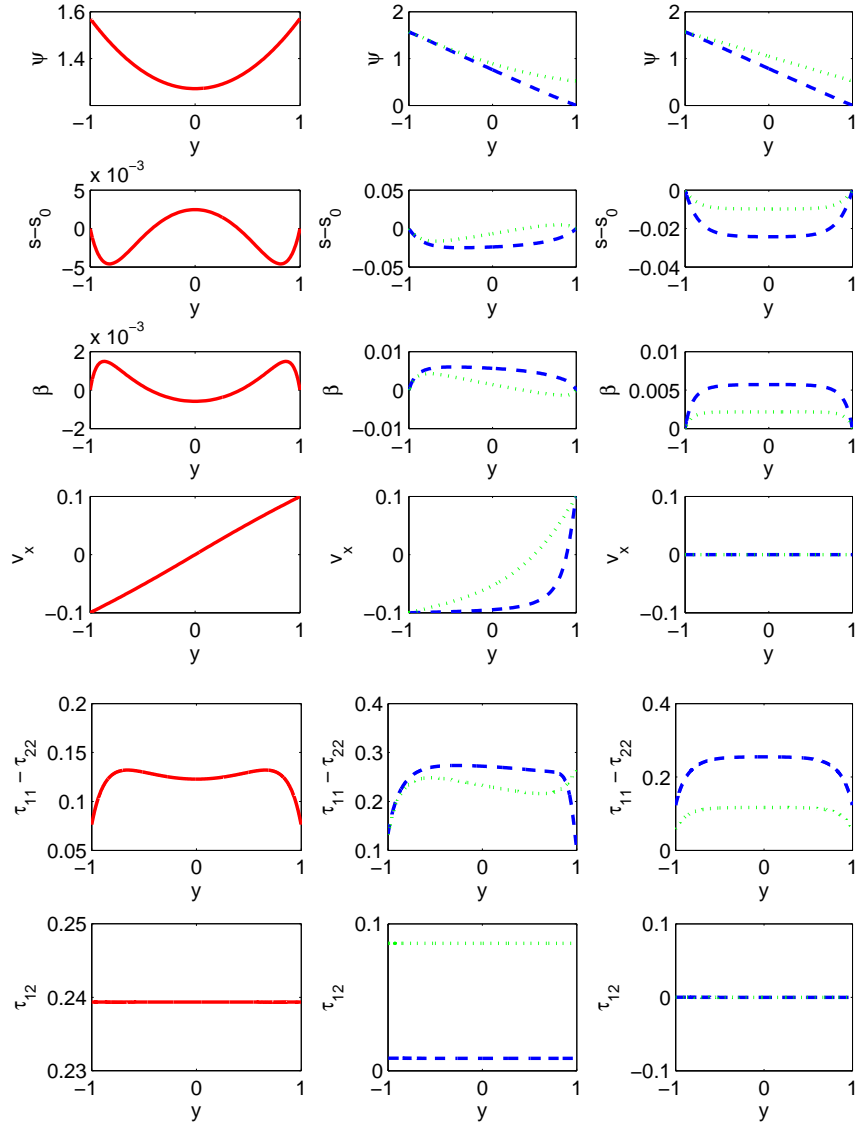
FIGURE 4. Couette flow structures, following Figures 1 and 2, except the lower plate is maintained throughout with homeotropic anchoring $\psi_0^- = \frac{\pi}{2}$. Column 1 is with identical anchoring at the top plate, with $De = 0.1$. Column 3 is the pure anchoring induced distortions without flow, Column 2 is the result with both slow flow and anchoring distortions, for two top plate anchoring conditions, $\psi_0^+ = \frac{\pi}{6}$ (dotted) and 0 (dashed). Rows 1-5 depict orientational, flow, and stress variables as in Figures 2,3.
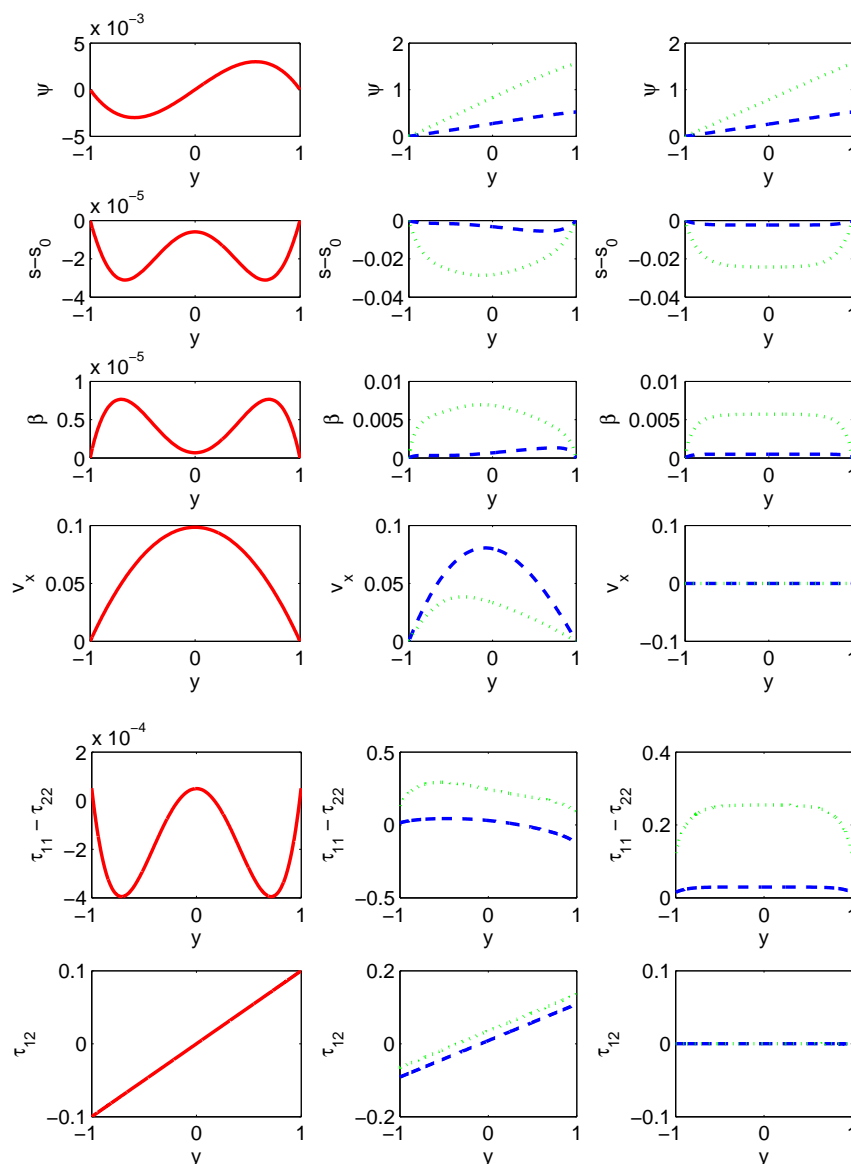
FIGURE 5. Gap structures for Poiseuille flow, with the same parameter studies as Figure 2 except the normalized plate speed De is replaced by the normalized pressure gradient ϵ. The lower plate anchoring condition is controlled at $\psi_0^- = 0$; Column 1 has identical top plate anchoring, whereas Columns 2 and 3 show results with anchoring mismatches, $\psi_0^+ = \frac{\pi}{6}$ (dashed) and $\frac{\pi}{2}$ (dotted). Columns 1 and 2 correspond to weak pressure gradient, $\epsilon = 0.1$, while Column 3 is the pure anchoring-induced distortion without flow, $\epsilon = 0$.
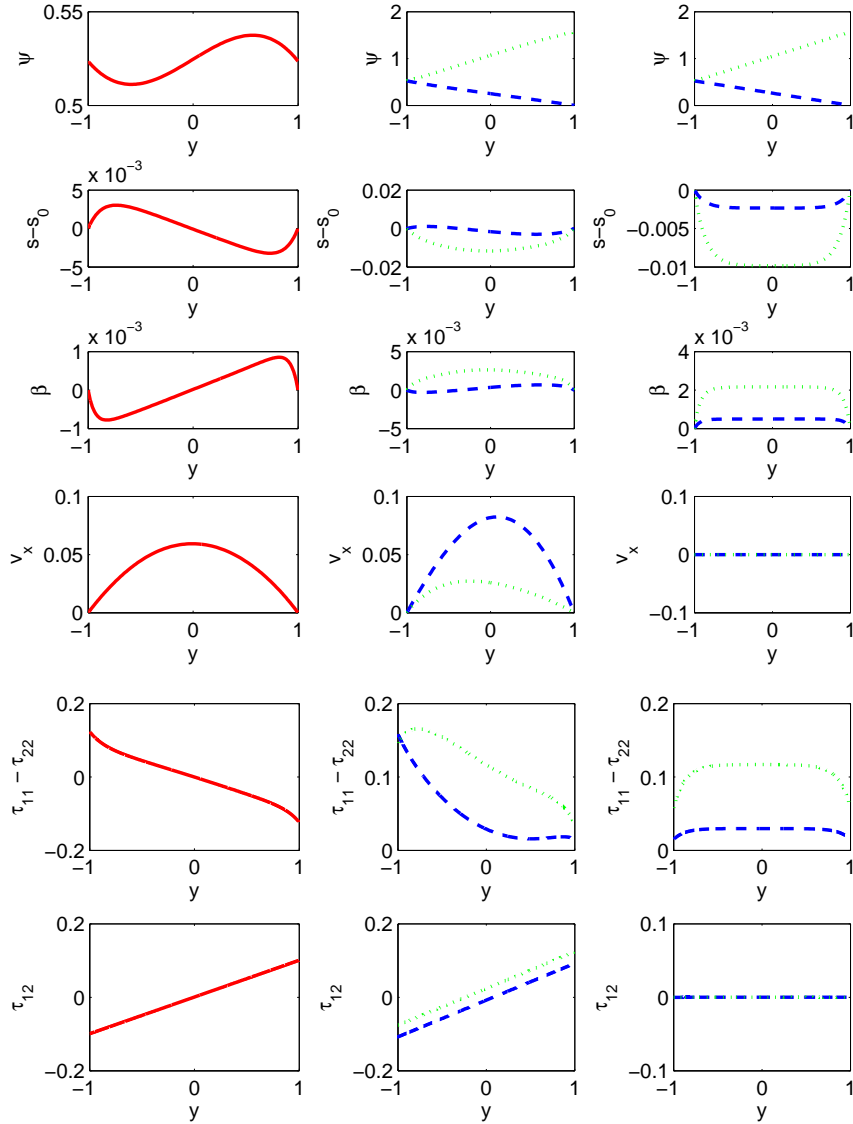
FIGURE 6.   Gap structures for the Poiseuille flow analog of Figure 3, with the weak pressure gradient ϵ replacing the weak plate speed De. The lower plate anchoring angle is tilted, $\psi_0^- = \frac{\pi}{6}$. Column 1 corresponds to identical plate anchoring at the top plate; Column 2 (with weak pressure gradient $\epsilon = 0.1$, top plate conditions $\psi_0^+ = 0$ (dashed) and $\frac{\pi}{2}$ (dotted) and Column 3 (with zero flow, $\epsilon = 0$, top plate conditions $\psi_0^+ = 0$ (dashed) and $\frac{\pi}{2}$ (dotted)), give results with anchoring distortions.
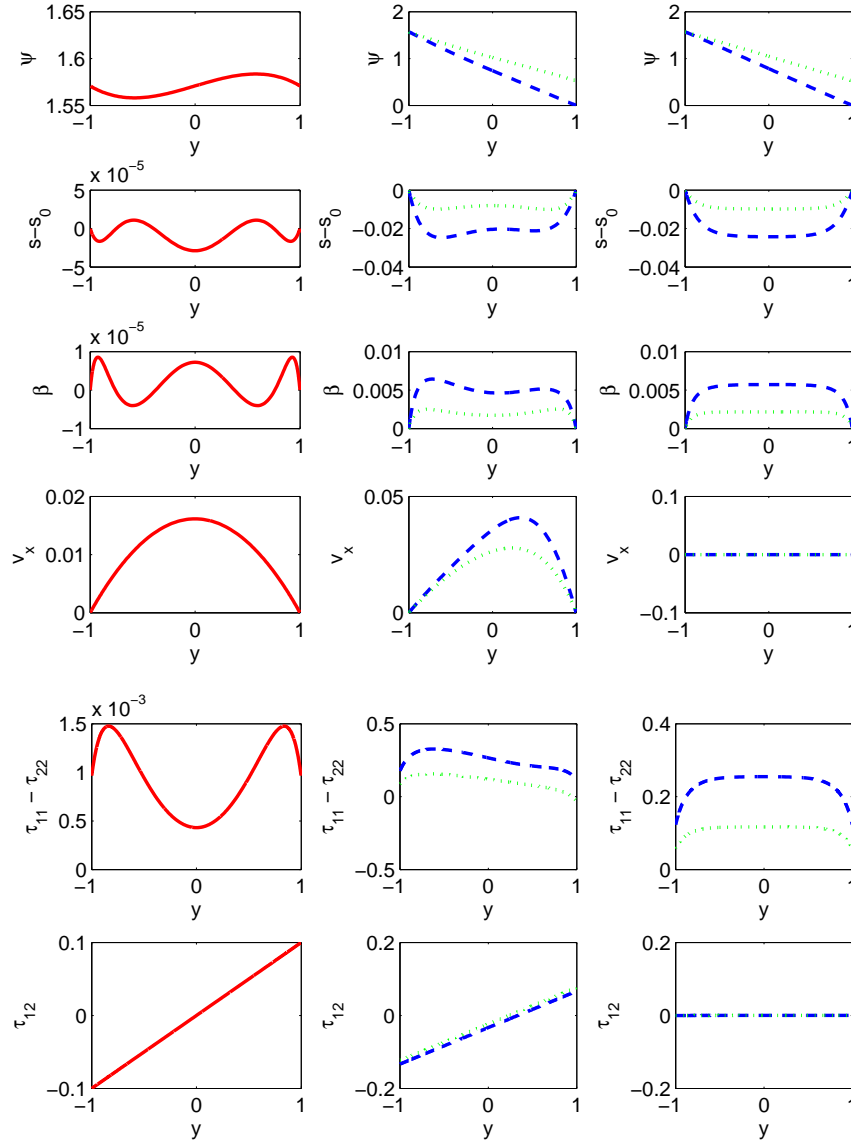
FIGURE 7. Gap structures for the Poiseuille flow analog of Figure 4, with homeotropic lower plate anchoring angle, $\psi_0^- = \frac{\pi}{2}$, weak pressure gradient $\epsilon = 0.1$ in Columns 1 and 2, and zero flow in Column 3. Column 1 corresponds to identical top and bottom plate anchoring conditions, while Columns 2 and 3 exhibit structures with anchoring mismatches, $\psi_0^+ = \frac{\pi}{6}$ (dotted) and 0 (dashed).